Reconstruction of $\not{E}_T$

- In general, $\not{E}_T$ is the negative of the vector sum of the transverse momenta of all final-state particles reconstructed in the detector
- CMS has developed three distinct algorithms to reconstruct
  - PF $\not{E}_T$,which is calculated using a complete particle-flow technique
    - $\sum E_T$ is the associated scalar sum of the transverse energies of the PF particles
  - Calo $\not{E}_T$, which is based on calorimeter energies and the calorimeter tower geometry,relative to the centre of the detector, to define pseudo-particles.
    - The $\not{E}_T$ excludes energy deposits below noise thresholds.
    - Since a muon deposits only a few GeV on average in the calorimeter, independent of its momentum, the muon pT is included in the Calo $\not{E}_T$ calculation

- TC $\not{E}_T$, which corrects Calo $\not{E}_T$ by including tracks reconstructed in the inner tracker after correcting for the tracks' expected energy depositions in the calorimeter
  - The predicted energy deposition for charged pions is used for all tracks not identified as electrons or muons.
  - The calorimetric energy deposit is estimated from simulations of single pions, in intervals of p_T and η, , and an extrapolation of the track in the CMS magnetic field is used to determine its expected position
  - No correction is applied for very high pT tracks (pT > 100 GeV), whose energy is already well measured by the calorimeters
  - For low-pT tracks (pT < 2 GeV) the measured momentum is taken into account assuming no response from the calorimeter.

Reason of The magnitude of the $\not{E}_T$ can be underestimated

- nonlinearity of the response of the calorimeter for neutral and charged hadrons due to its noncompensating nature,
- neutrinos from semileptonic decays of particles
- minimum energy thresholds in the calorimeters
- pT thresholds and inefficiencies in the tracker
- for Calo $\not{E}_T$ charged particles that are bent by the strong magnetic field of the CMS solenoid and whose calorimetric energies are therefore in a calorimeter cell whose associated angle is very different from the angle of the track at the vertex.

A TWO-STEP CORRECTION HAS BEEN DEVISED IN ORDER TO REMOVE THE BIAS

- type-I corrections use these jet energy scale corrections for all jets that have less than 0.9 of their energy in the ECAL and corrected pT > 20 GeV for Calo $\not{E}_T$, and for a user-defined selection of jets with pT > 10 GeV for PF $\not{E}_T$
- type-II correction
  - In order to correct the remaining soft jets below this threshold, and energy deposits not clustered in any jet, a second correction can be applied to the unclustered energy

Introduction to Jet Energy Corrections

- The calorimeter response to particles is not linear and therefore it is not straightforward to translate the measured jet energy to the true particle or parton energy.
- The **jet corrections** are a set of tools that allows the proper mapping of the measured jet energy deposition to the analysis desired level

Factorized Approach

- CMS has adopted a **factorized** solution to the problem of jet energy corrections, where each level of correction takes care of a different effect.
- **L1 Pile Up** The goal of the L1 correction is to remove the energy coming from pile-up events. In principle this will remove any dataset dependence on luminosity so that the following corrections are applied upon a luminosity independent sample.
- **L2 Relative Jet Correction** The goal of the L2 Relative correction is to make the jet response flat vs eta. Essentially, the uniformity in pseudorapidity is achieved by correcting a jet in arbitrary eta relative to a jet in the central region (|eta|<1.3). The derivation of the Relative correction is done either by using MC truth or by employing a data driven method (*dijet balance*).

- **L3 Absolute Jet Correction** The goal of the L3 Absolute correction is to make the jet response flat vs pt. Once a jet has been corrected for eta dependence (L2 relative correction), it is corrected *back to particle level* (this means that the corrected CaloJet pt is equal **on average** to the GenJet pt). The derivation of the Absolute correction is done either by using MC truth information or by employing data driven techniques (*Z/gamma+jet balance*).
- **L4 EMF (electromagnetic energy fraction) Jet Correction** The goal of the optional L4 EMF jet correction is to make the jet response uniform vs the electromagnetic energy fraction (EMF). It is a residual correction on top of the default L2+L3 and it has been shown to improve the jet resolution.

- **L5 Jet Flavor Correction** The goal of the optional L5 Flavor jet correction is to correct for the jet flavor dependence. It is applied on top of the default L2+L3 jet correction and corrects back to the particle level.
- The L2+L3 corrections scale the energy of an "average QCD jet" back to the energy of the corresponding generator level particle jet. However, an analysis of the individual jet flavors (uds, c, b, gluon) shows that different corrections are needed for different jet flavors. This leads to an over- or undercorrection if the L2+L3 corrections are applied to jets with a flavor composition different than that of QCD jets. For example, jets from the hadronic decay of a W boson consist only of uds and c quarks, which have a higher energy response than b and gluon jets. Consequently, applying L2+L3 corrections to these jets will result in an overcorrection. A first pass of flavor-specific corrections is provided as a a tool to minimize the flavor-dependence of the L2+L3 corrections.The L5 corrections act at the particle level. If corrections back to the parton level are required (for example, when reconstructing the Z or W mass in their hadronic decays), the L2+L3+L5 corrections can be combined with the L7 corrections.

- **L7 Parton Jet Correction** The optional L7 parton correction is applied **on top of** the default L2+L3 correction and corrects back to the parton level, which means that the corrected CaloJet pt is equal to the originating parton pt on average.
- The L7 correction function has been calculated comparing the GenJet transverse momentum to the matched parton ($\Delta R<0.15$). Physics definition of the GenJet flavour has been used
- There are 5 jet algorithms: iterative cone $\Delta R=0.5$ (IC5), KT jet D=0.4 and 0.6 (KT4 and KT6) and SisCone $\Delta R=0.5$ and 0.7 (SC5 and SC7). For each algorithm 9 different functions are available:
  - flavour: 0 gluons from diJet
  - flavour: 1 light quark from diJet
  - flavour: 2 charms from diJet
  - flavour: 3 beauty from diJet
  - flavour: 4 soup from diJet
  - flavour: 5 light quark from ttbar
  - flavour: 6 charms from ttbar
  - flavour: 7 beauty from ttbar
  - flavour: 8 soup from ttbar

Large $\not{E}_T$ due to misreconstruction

- Contributions to $\not{E}_T$ from anomalous signals in the calorimeters
  - The CMS ECAL and HCAL occasionally record anomalous signals that correspond to particles hitting the transducers.
  - Anomalous signals in HCAL can also be produced by rare random discharges of the readout detectors.

Removal of beam-induced contributions to $\not{E}_T$

- Machine-induced backgrounds, especially the production of muons when beam protons suffer collisions upstream of the detector
- The CMS beam-halo event filter uses trigger and reconstruction-level information obtained from the Cathode Strip Chambers , a subdetector with good reconstruction performance for both collision and non-collision muons and can be used to tag events for removal
- Beam-halo muons, because their tracks do not point towards the nominal interaction point in the centre of the detector, in general do not fire the triggers for muons from pp interactions

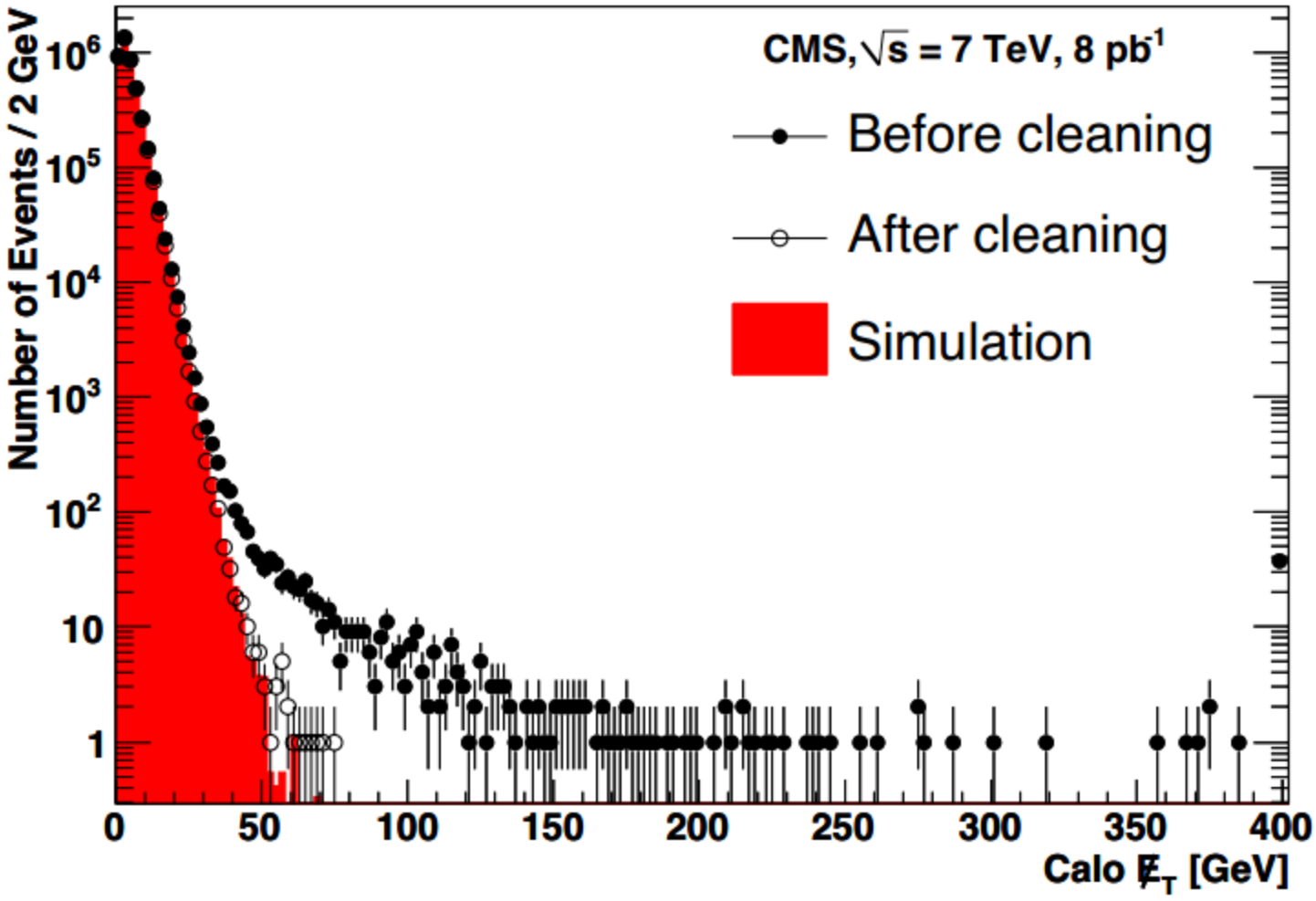

Figure 1: Calo $\not\!\!E_T$ distributions in a minimum bias data sample without (black dots) and with (open circles) cleaning and filters, compared to simulation. Overflows are included in the highest bin.

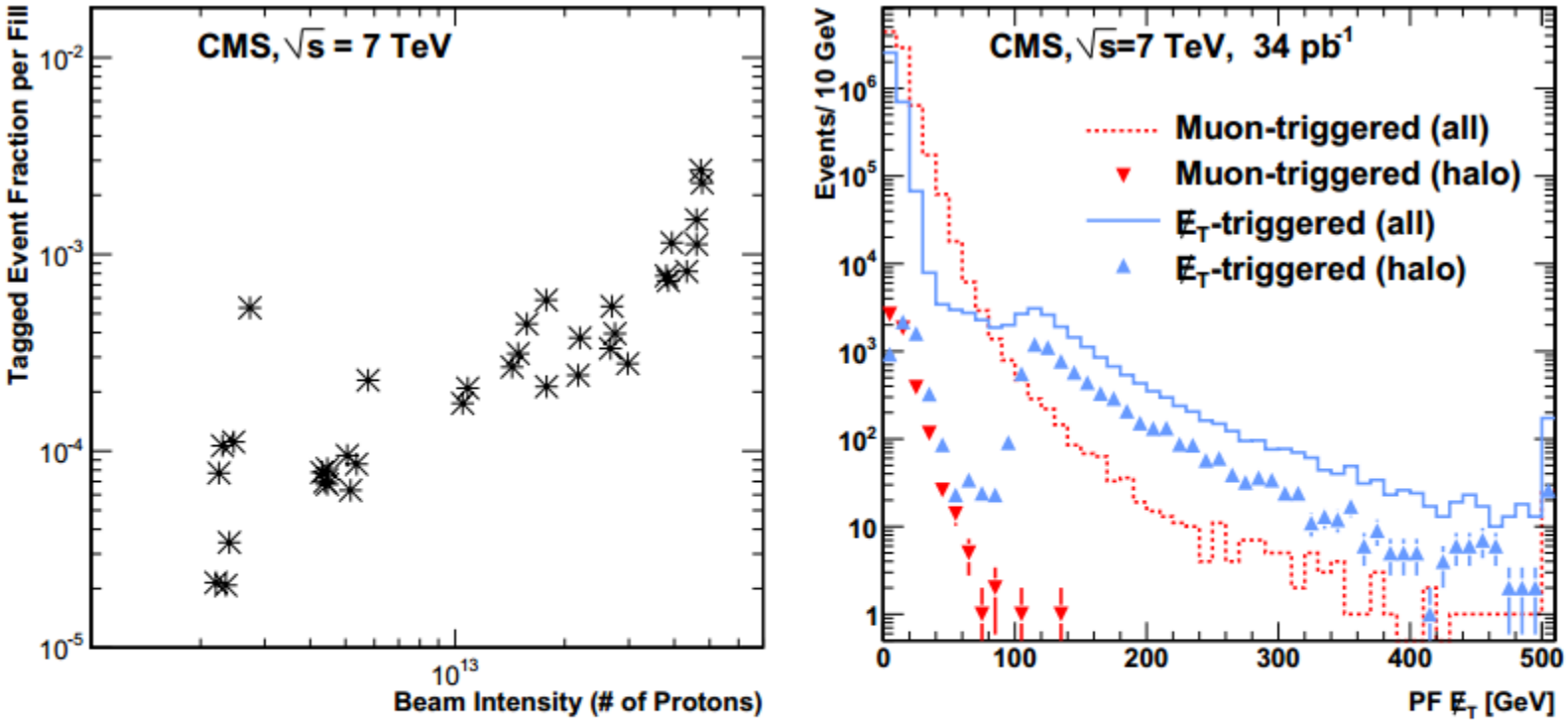

Figure 2: (left) Probability of finding a beam-halo tagged event in muon-triggered events. Results are shown as a function of the beam intensity. (right) PF $\not\!\!E_T$ distribution for all the events from muon and Calo $\not\!\!E_T$ triggers that were analyzed, and for the subset of these events that were identified as beam halo.

- The distribution from events recorded by collision muon triggers is shown by the dashed curve while that of the subset of these events which met the requirements of the tight halo filter is shown by the red inverted triangles

- Contributions of non-instrumented or non-functioning detector regions
  - Particles traversing poorly instrumented regions of the detector can be a cause of apparent $\not{E}_T$
  - While generally hermetic, the CMS calorimeter does have uninstrumented areas (cracks) at the boundary between the barrel and endcap sections, and between the endcap and the forward calorimeters.
    - The gap between the barrel and endcap sections is about 5 cm and contains various services, including cooling, power cables, and silicon detector readout

- In addition, about 1% of the ECAL crystals are either not operational or have a high level of electronic noise , and they are masked in reconstruction

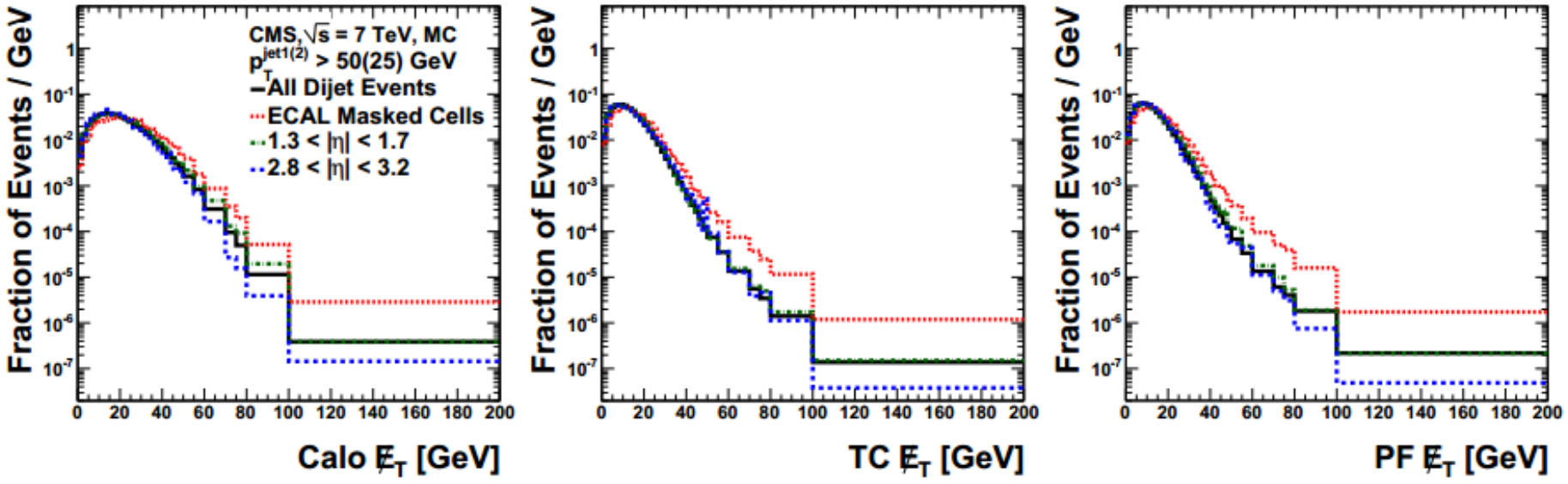

Figure 4: Distribution of (left) Calo $\not\!\!E_{\mathrm{T}}$, (middle) TC $\not\!\!E_{\mathrm{T}}$, and (right) PF $\not\!\!E_{\mathrm{T}}$, normalized to unit area, for events containing at least 2 jets with $p_{\mathrm{T}}^{\mathrm{jet1(2)}} > 50$ (25) GeV (black solid), and for the subsets of these events with a jet aligned with $\vec{\not\!\!E}_{\mathrm{T}}$ within $\Delta\phi(\vec{\not\!\!E}_{\mathrm{T}}, \mathrm{jet}) < 0.2$ and pointing towards a masked ECAL cell (red dotted), the barrel-endcap boundary (green dot-dashed), and the endcap-forward boundary (blue dashed) in simulation.

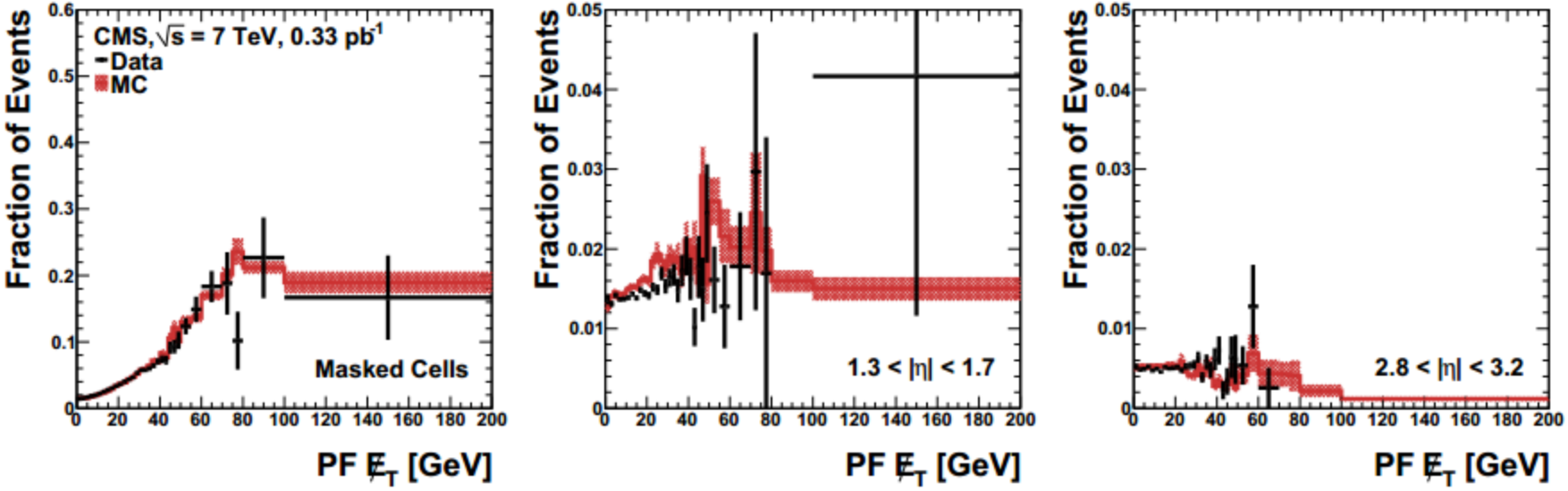

Figure 5: Fraction of dijet events in data (points) and simulation (red band) with a jet aligned to $\vec{\not\!\!E}_T$ within $\Delta\phi(\vec{\not\!\!E}_T, \text{jet}) < 0.2$ and pointing towards (left) a masked ECAL channel, (middle) the barrel-endcap boundary, and (right) the endcap-forward boundary, in data and in simulation.

- As shown in Figs. 5(middle) and 5(right), the fraction of events which contain a jet that is both aligned with the $\not\!\!E_T$ and pointing towards a calorimeter boundary does not have a strong dependence on $\not\!\!E_T$
- the masked ECAL channels enhance the rate of events with large $\not\!\!E_T$
- Results from simulations indicate that the fraction of events with large $\not\!\!E_T$ due to mismeasurements

Missing transverse energy scale and resolution

- Events containing vector bosons may be produced in hard parton-parton collisions such as

  $qg \rightarrow q\gamma$, $q\bar{q} \rightarrow Z$, $qg \rightarrow qZ$, and $q\bar{q} \rightarrow gZ$.

- While there is no genuine $\not\!\!E_T$ in these events, we can induce it by removing the vector boson.
- The following notation is used: the vector boson momentum in the transverse plane is $\vec{q}_T$,
- the vector sum of the transverse momenta of all particles except the vector boson is $\vec{u}_T$.
- $\vec{q}_T + \vec{u}_T = 0.$

DIRECT PHOTON SAMPLE

- Candidate photon events are selected by requiring each event to contain exactly one reconstructed photon in the barrel portion of the ECAL , with qT > 20 GeV
- About half of the observed rate arises from QCD dijet production.Such jets are typically highly enriched in $\pi^0 \rightarrow \gamma\gamma$ and contain little hadronic activity

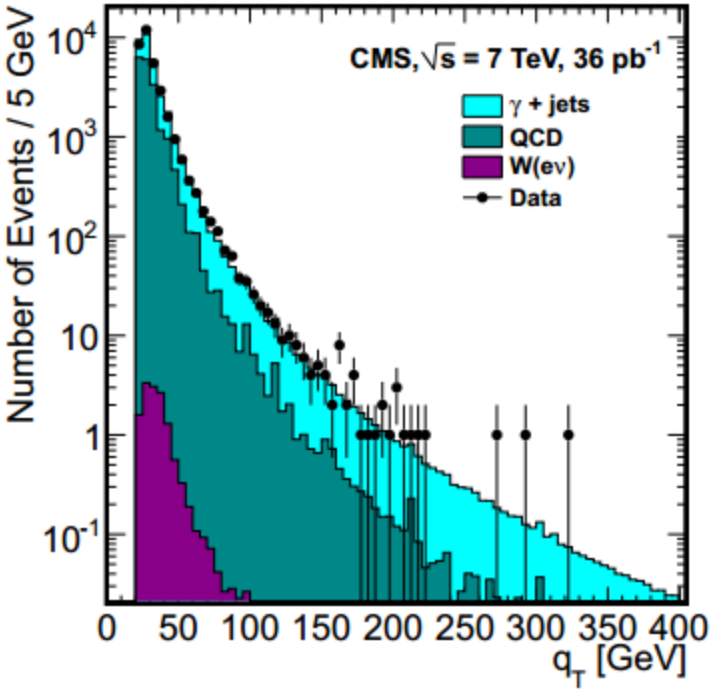

Figure 6: Distribution of q_T for events selected as photon+jet candidates. Predicted rates from simulation for signal and backgrounds are also shown. QCD refers to multijet events.

Z SAMPLES

For the $Z \rightarrow e^+e^-$ selection (electron channel), we require two well-identified and isolated electrons, with $p_T > 20$ GeV, within the fiducial region of the ECAL. The invariant mass ($M_{\ell\ell}$) of the electron pair is required to be in the range $70 < M_{\ell\ell} < 120$ GeV.

For the $Z \rightarrow \mu^+\mu^-$ selection (muon channel), we require two isolated muons with opposite electric charges, that have $p_T > 20$ GeV, and are within the $|\eta| < 2.1$ region. The invariant mass $M_{\ell\ell}$ of the muon pair is required to be at least 60 GeV, and no more than 120 GeV.

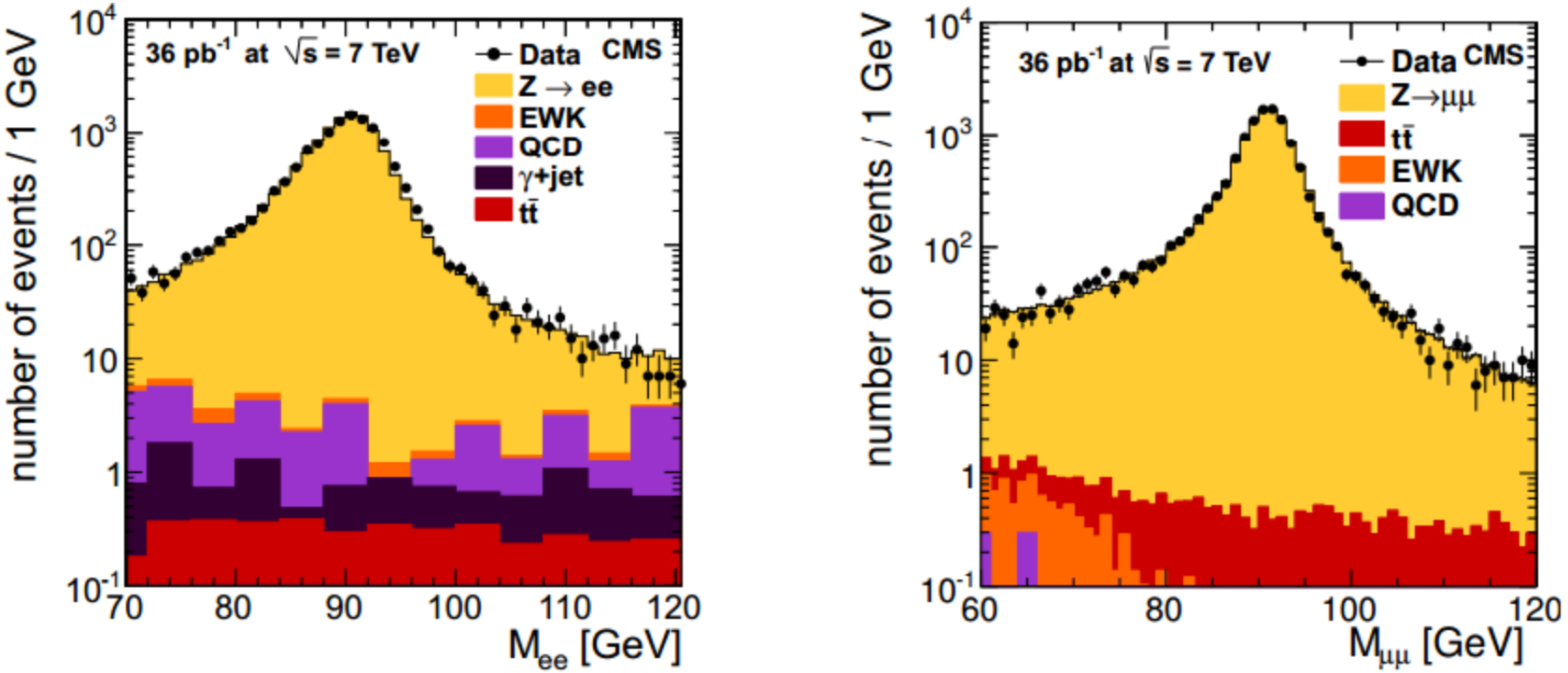

Figure 7: (left) Invariant mass distribution of the two leading electrons and (right) invariant mass distribution of the two leading muons, for the Z boson candidates, along with the predicted distribution from simulation. QCD refers to multijet events.

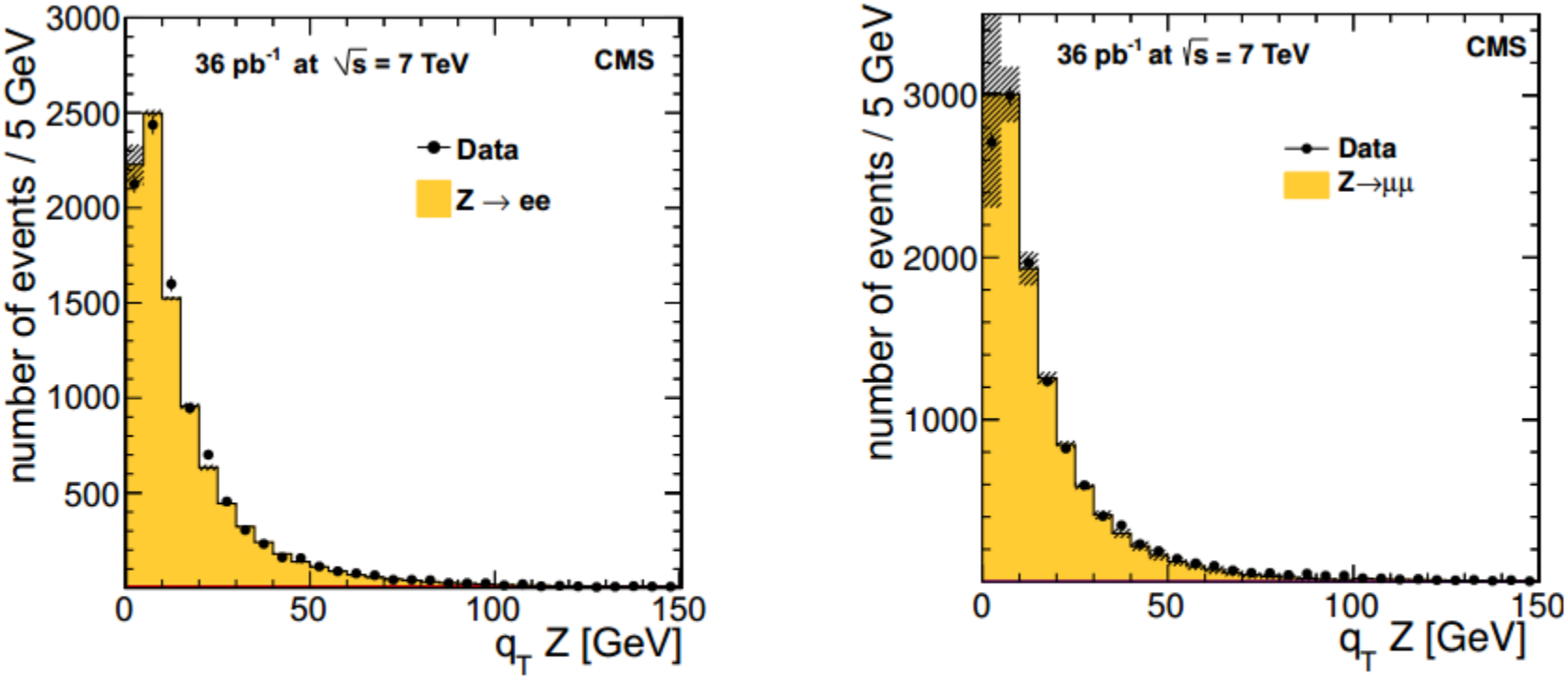

Figure 8: The q_T distribution for Z boson candidates in (left) the electron channel and (right) the muon channel, along with the prediction from simulation. Systematic uncertainties are shown as grey bands.

Scale and resolution for events with one primary vertex

- parallel component is mainly negative

$$u_{\parallel} \equiv \vec{u}_{\mathrm{T}} \cdot \hat{q}_{\mathrm{T}}$$

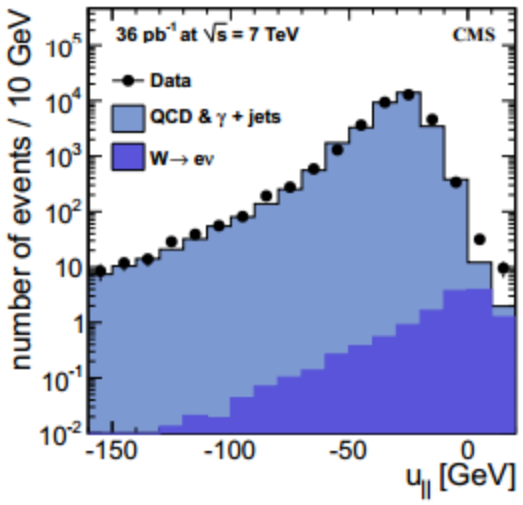

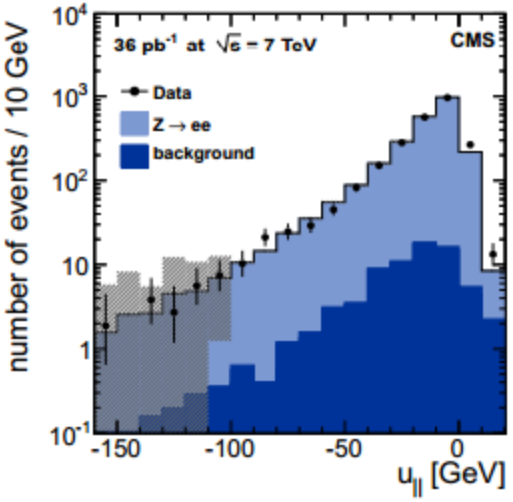

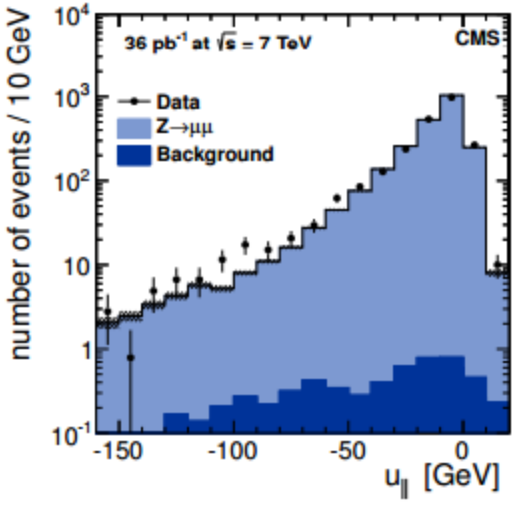

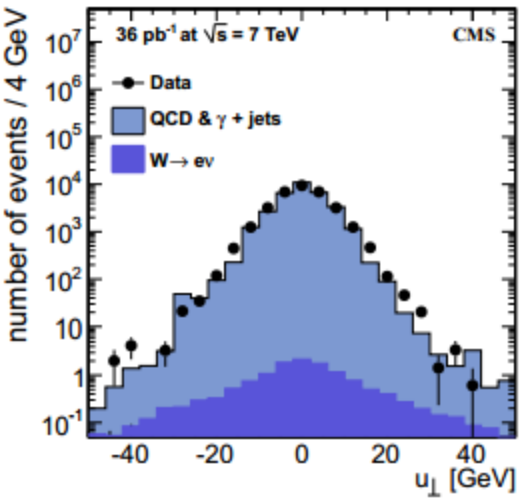

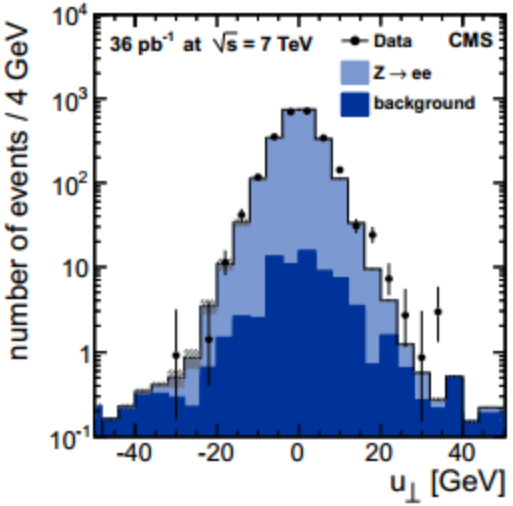

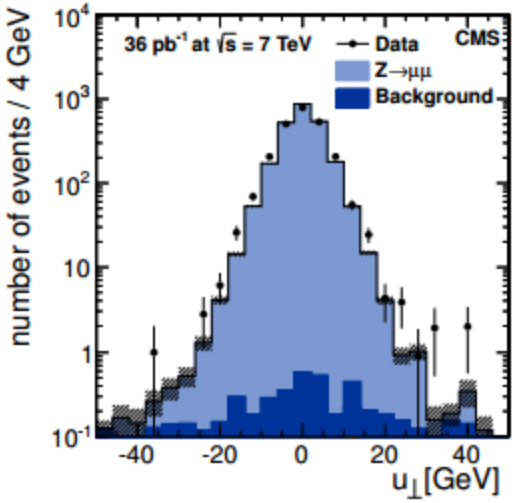

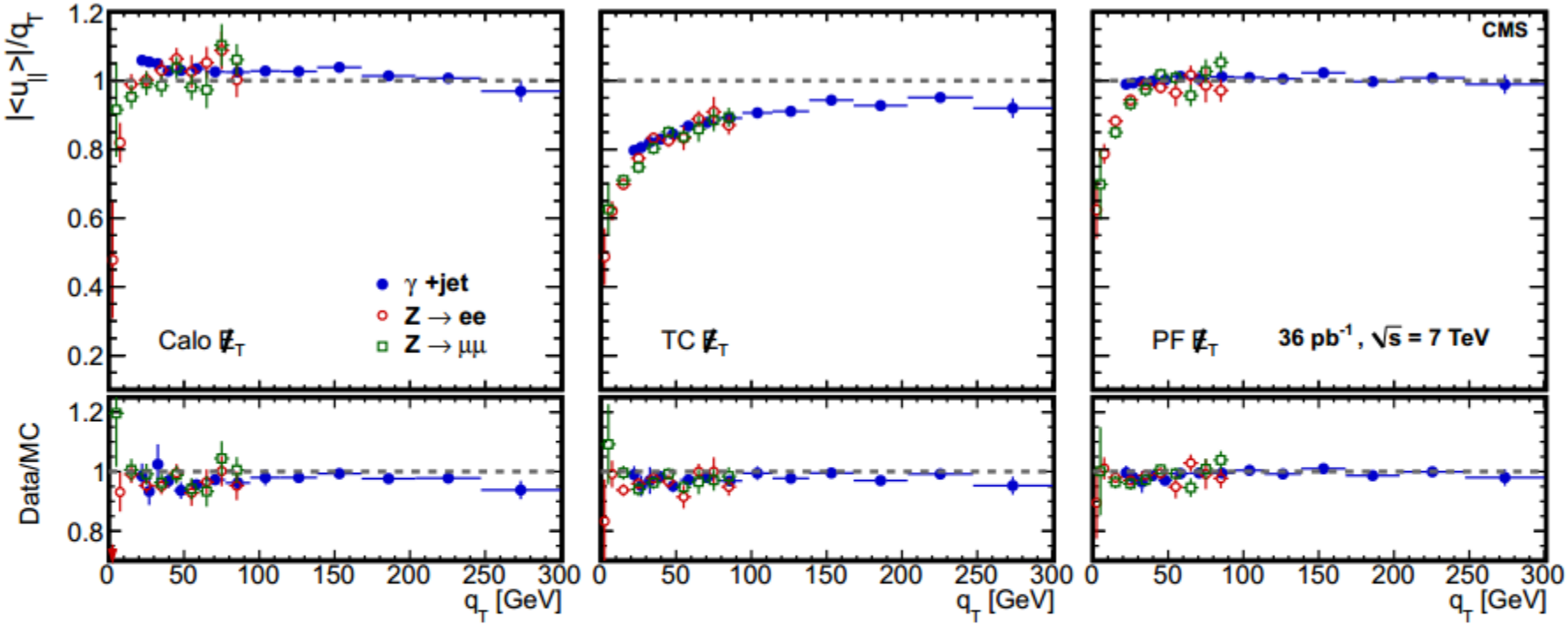

Figure 10: Response curves for events with one primary vertex, for (left) Calo $\not\!\!E_T$, (middle) TC $\not\!\!E_T$, and (right) PF $\not\!\!E_T$. Results are shown for photon events (full blue circles), $Z \to e^+e^-$ events (open red circles) and $Z \to \mu^+\mu^-$ events (open green squares). The upper frame of each figure shows the response in data; the lower frame shows the ratio of data to simulation. The vertical axis labels at the far left apply to all three subfigures.

- The response for Calo $\not{E}_T$ is slightly larger than one because the jet energy scale used in the type-I corrections was determined from a sample with a mixture of quark and gluon jets, while for these samples the leading jet is primarily a quark jet
- The TC $\not{E}_T$ response is lower because it has neither type-I nor type-II corrections.
- The PF $\not{E}_T$ response is lower than the Calo $\not{E}_T$ response at low values of qT because Calo $\not{E}_T$ has type-II corrections while PF $\not{E}_T$ has only type-I corrections.

- Because the $\not\!\!E_T$ resolution has a strong resolution has a strong $\sum E_T$, it is presented as a function of $\sum E_T$.
- In order to make a meaningful comparison, we calibrate the measured $\not\!\!E_T$ for the different algorithms to the same scale

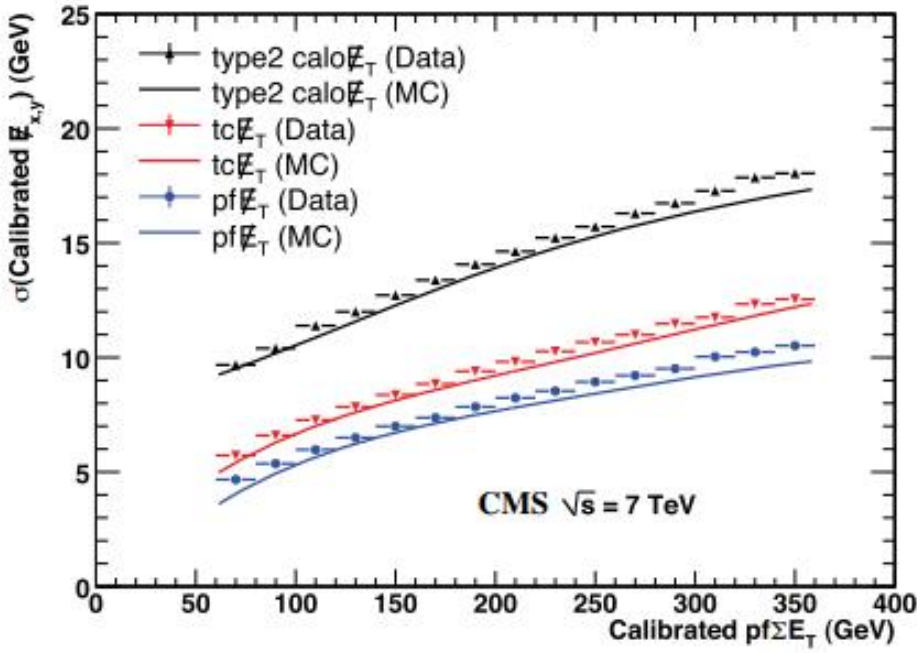

Figure 13: Calibrated $\not\!\!E_{x,y}$ resolution versus calibrated PF $\sum E_T$ for Calo $\not\!\!E_T$, TC $\not\!\!E_T$, and PF $\not\!\!E_T$ in data and in simulation.

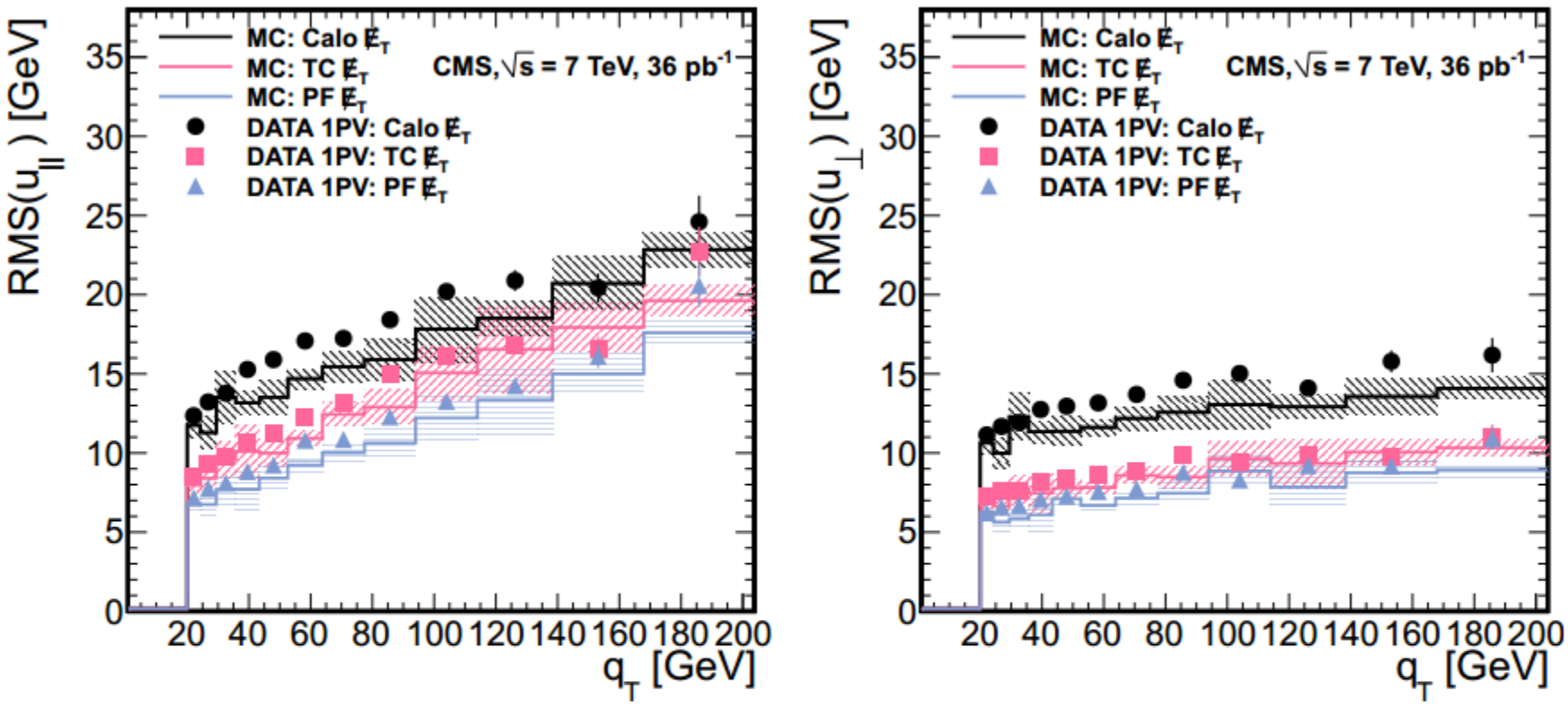

Figure 11: Resolution curves for components of hadronic recoil measured in direct photon candidate events with one primary vertex. (left) parallel to boson; (right) perpendicular to boson. Data and simulation are indicated by points and histograms, respectively. Black circles (upper): Calo $\not\!\!E_T$; Pink squares (middle): TC $\not\!\!E_T$; Blue triangles (bottom): PF $\not\!\!E_T$. Shaded regions indicate statistical uncertainties on the simulation.

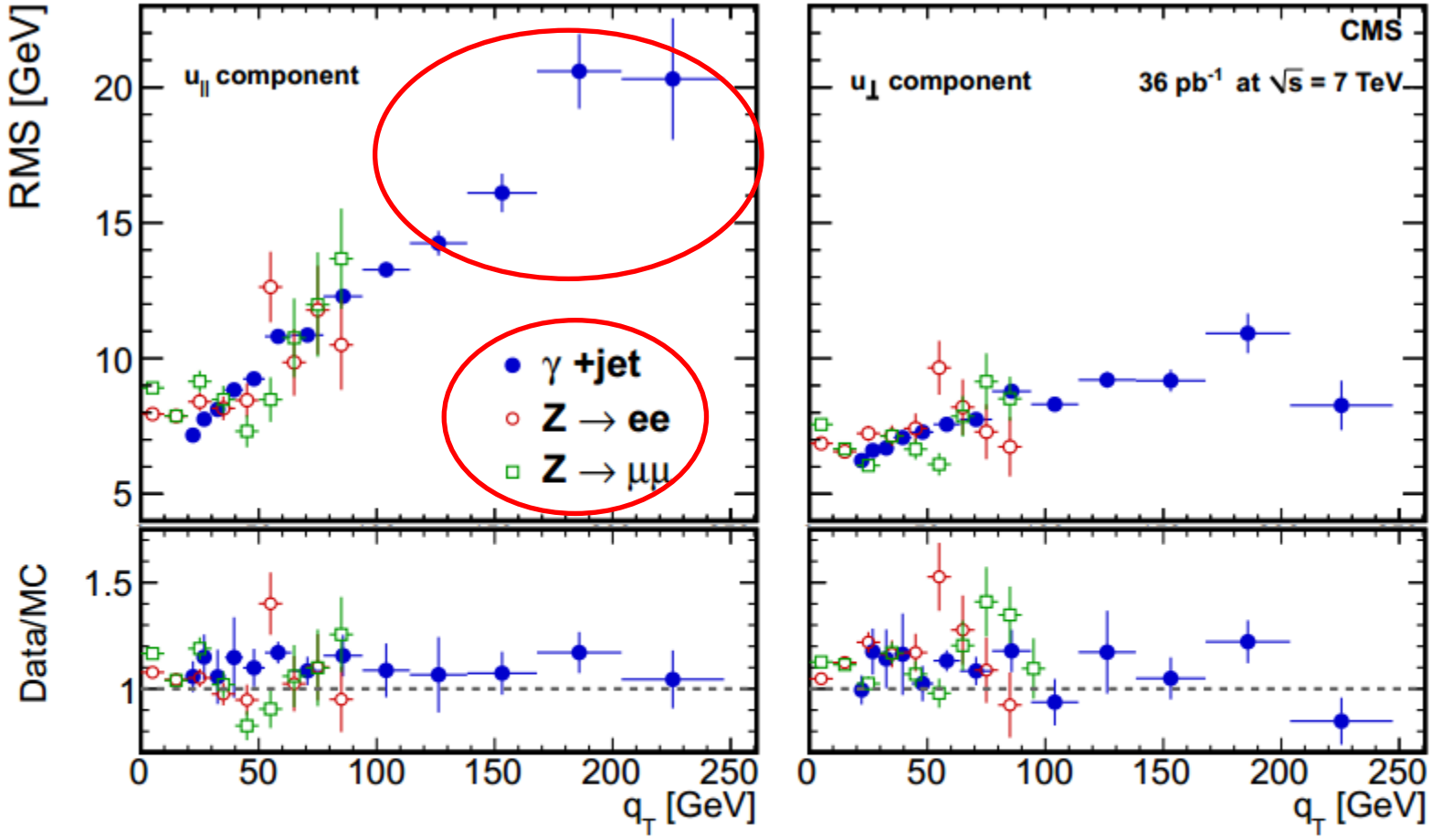

Figure 12: Resolution curves for components of hadronic recoil calculated using PF $\not\!\!E_T$ measured in events with one primary vertex. Left: parallel to boson; right: perpendicular to boson. $Z \to \mu^+\mu^-$, $Z \to e^+e^-$ and γ events are indicated by open green squares, open red circles and full blue circles, respectively. The lower frame indicates the ratio of data to simulation. The vertical axis labels at the far left apply to both subfigures.

Studies of pile-up effects using photon and Z events

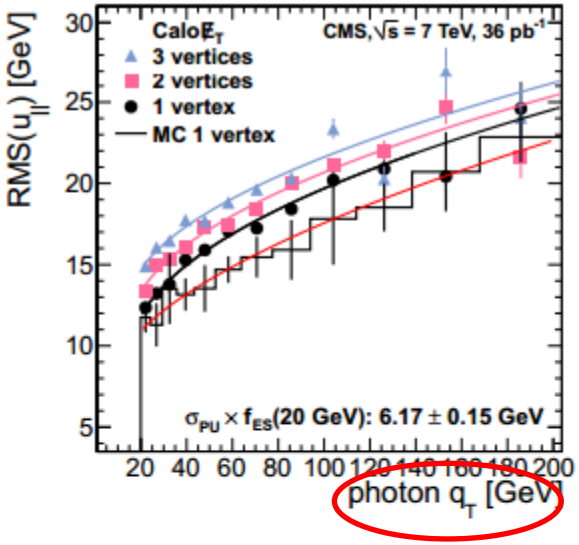

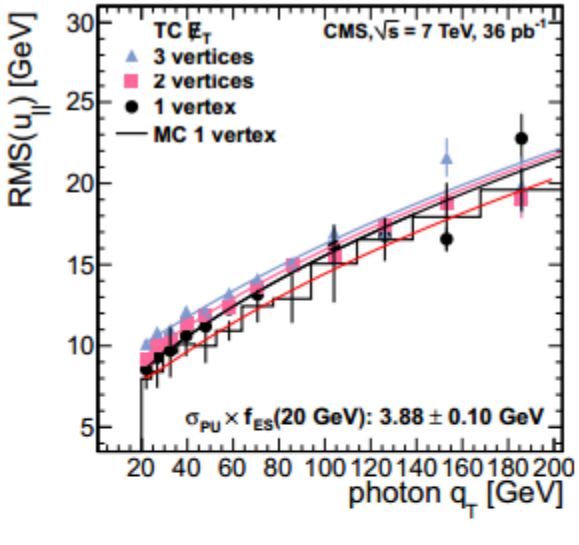

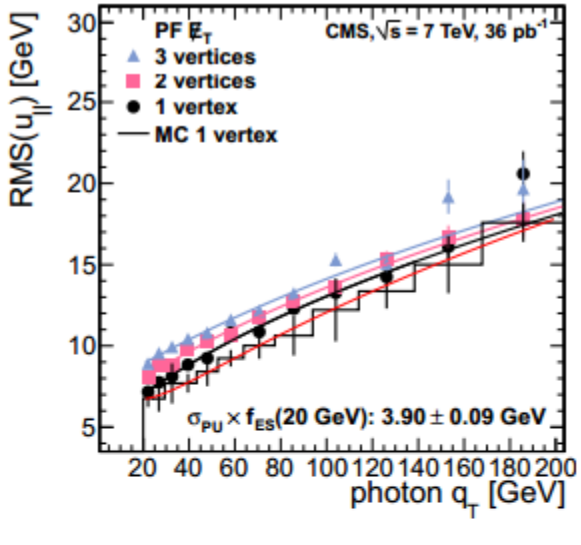

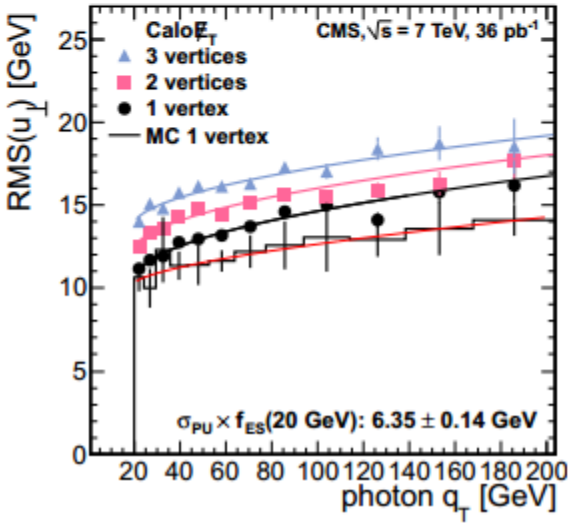

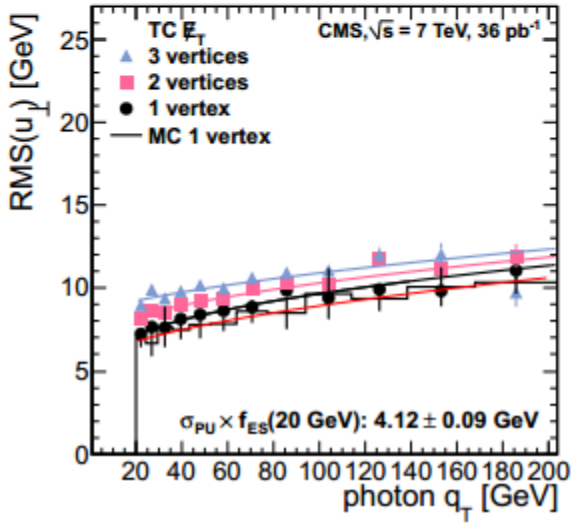

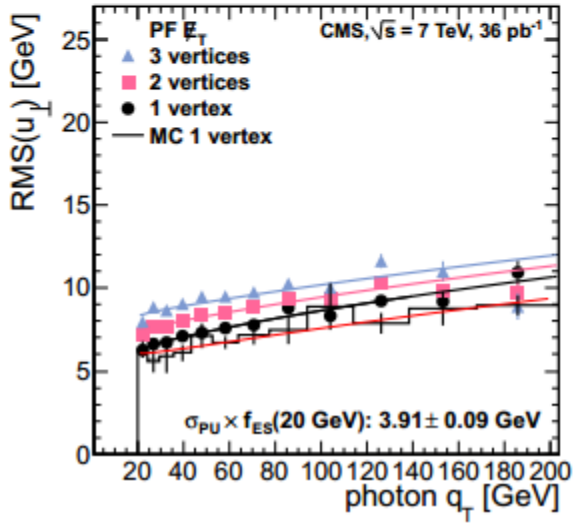

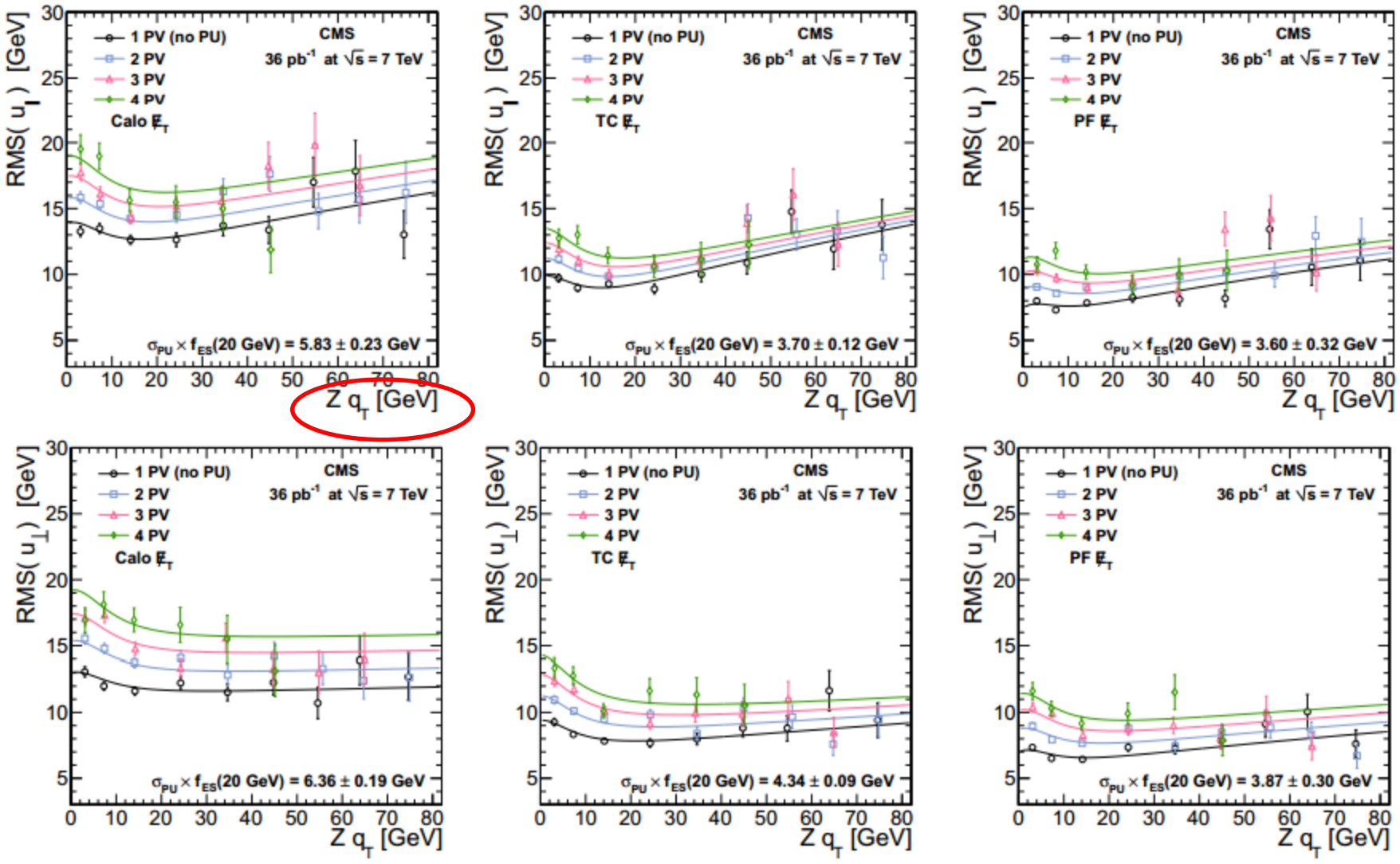

Figure 17: Resolution versus the q_T of the Z for the parallel component (top) and perpendicular component (bottom) for (left to right) Calo $\not\!\!E_T$, TC $\not\!\!E_T$, and PF $\not\!\!E_T$, for events with 1 (circles), 2 (squares), 3 (triangles), and 4 (diamonds) reconstructed primary vertices.

The parameterization of $\not{E}_T$ resolution used in Figs. 16 and 17 is given by :

$$\sigma^2_{\text{total}} = (a\sqrt{q_T} + b)^2 + (\sigma_{\text{noise}} f_{ES}(q_T))^2 + (N-1)(\sigma_{PU} f_{ES}(q_T))^2 \quad (1)$$

where a and b characterize the hard process, σ_{noise} is the intrinsic noise resolution, N is the number of reconstructed vertices in the event, σ_{PU} is the intrinsic pile-up resolution, and $f_{ES}(q_T)$ is the energy scale correction applied on each event. At low q_T, the resolution is dominated by

- At low qT, the resolution is dominated by contributions from the underlying event and detector noise (σ_{noise}).

W EVENTS

The performance of $\not\!\!E_T$ is studied in events that contain large, genuine $\not\!\!E_T$: $W \to \ell\nu$ events, where ℓ is a muon or electron. For most W events, the magnitude of $\vec{\not\!\!E}_T$ is approximately equal to the p_T of the charged lepton, but its resolution is dominated by the hadronic recoil. When the W q_T is small compared to the W mass, the $\not\!\!E_T$ is approximately

$$\not\!\!E_T \approx p_T(\ell) - 0.5u_\ell$$

where u_ℓ is the component of the recoil parallel to the lepton transverse direction.

- Recoil: one of the highest systematic uncertainties on width

$W \rightarrow e\nu$ decays

- A single-electron high-level trigger requirement with a pT threshold of 15 GeV is applied.
- Events are also required to contain an electron with pT > 25 GeV. Events with a second electron with pT > 20 GeV are rejected, and rejection against γ conversions is applied.

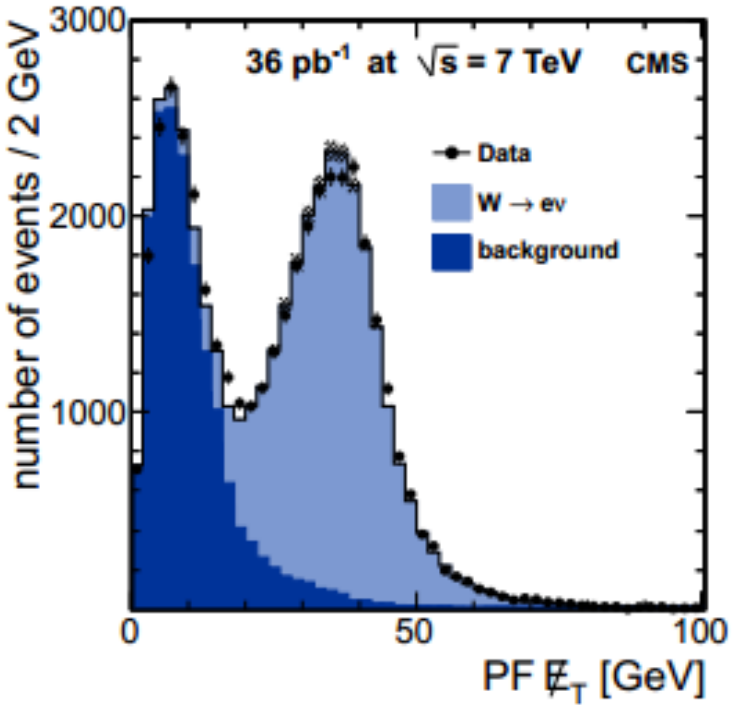

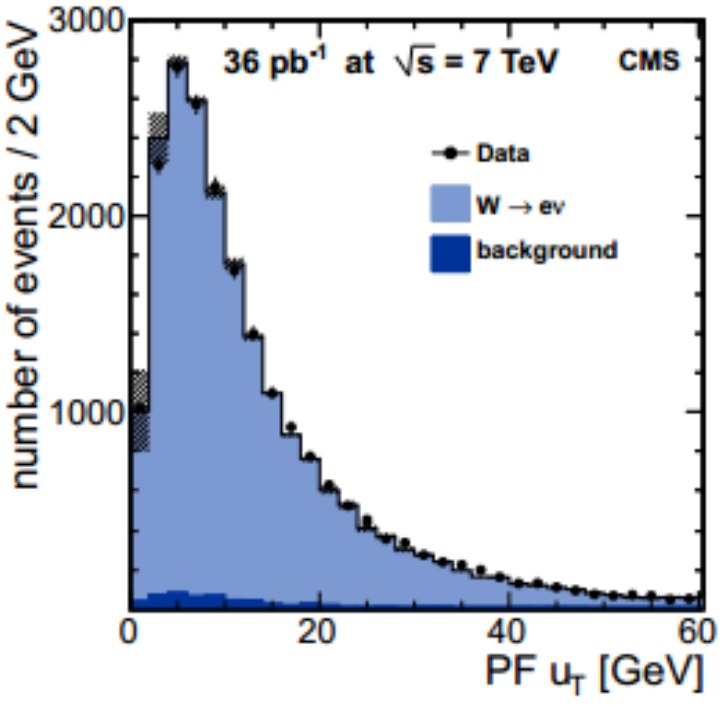

$W \rightarrow \mu\nu$ decay

- events are required to have been collected by a single-muon high-level trigger
- In addition, candidates are selected by requiring a muon with $|\eta| < 2.1$ that has pT > 25 GeV.
- Events with a second muon with pT > 25 GeV are rejected to suppress Z and $t\bar{t}$ contamination.

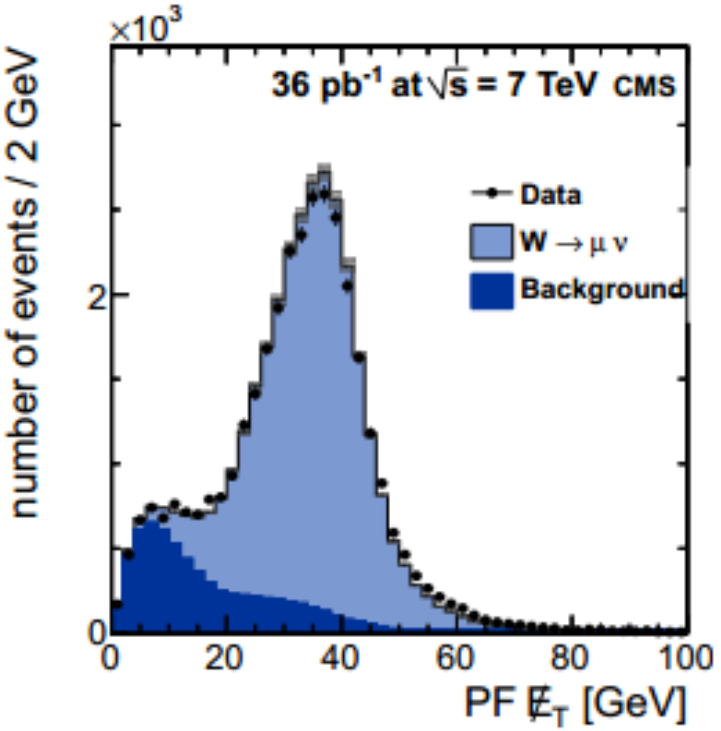

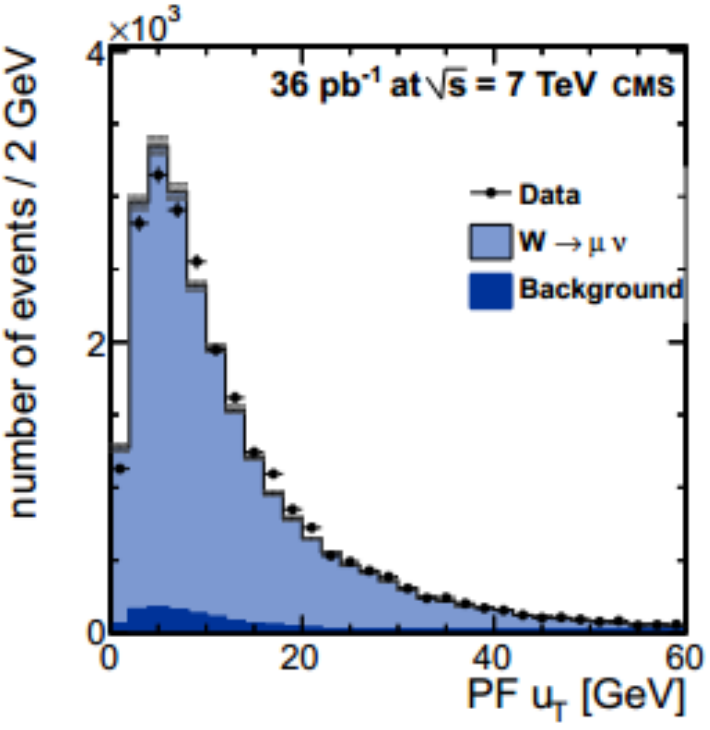

SOURCES OF BACKGROUND

- The mainsources of background
  - jet events with one jet falsely identified as a high-pT muon
  - $Z \to \ell\ell$ events with one lepton escaping detection
- Other backgrounds include
  - W and Z bosons decaying into τ, followed by $\tau \to \ell\nu\bar{\nu}$,
  - $t\bar{t}$ events, with one top quark decaying semileptonically

$\not{E}_T$ SIGNIFICANCE

- $$\vec{E}_T^{\,\text{total}} = \sum_{i \in X} \vec{E}_{T_i} = -\vec{\not{E}}_T,$$
- the likelihood function is given by

$$\begin{aligned}
\mathcal{L}(\vec{\varepsilon}) &= \int P_1(\vec{E}_{T_1}|\vec{e}_{T_1}))P_2(\vec{E}_{T_2}|\vec{e}_{T_2}))\delta(\vec{\varepsilon} - (\vec{E}_{T_1} + \vec{E}_{T_2}))\, d\vec{E}_{T_2}\, d\vec{E}_{T_2} \\
&= \int p_1(\vec{\varepsilon}_1|\vec{e}_{T_1})p_2(\vec{\varepsilon}_2|\vec{e}_{T_2})\delta(\vec{\varepsilon} - (\vec{\varepsilon}_1 + \vec{e}_{T_1} + \vec{\varepsilon}_2 + \vec{e}_{T_2}))\, d\vec{\varepsilon}_1\, d\vec{\varepsilon}_2 \\
&= \int p_1(\vec{\varepsilon}_1|\vec{e}_{T_1})p_2(\vec{\varepsilon}_2|\vec{e}_{T_2})\delta(\vec{\varepsilon} - (\vec{\varepsilon}_1 + \vec{\varepsilon}_2))\, d\vec{\varepsilon}_1\, d\vec{\varepsilon}_2,
\end{aligned}$$

  - $\vec{e}_{T_i}$, , the true transverse momentum of the object
  - $\vec{E}_{T_i}$ the measured transverse momentum of the object
- The significance is defined as

$$\mathcal{S} \equiv 2 \ln \left(\frac{\mathcal{L}(\vec{\varepsilon} = \sum \vec{\varepsilon}_i)}{\mathcal{L}(\vec{\varepsilon} = 0)} \right),$$

$$p_i(\vec{\varepsilon}_i|\vec{e}_{\mathrm{T}_i}) \sim \exp\left(-\frac{1}{2}(\vec{\varepsilon}_i)^T \mathbf{V}_i^{-1}(\vec{\varepsilon}_i)\right),$$

$$\mathcal{L}(\vec{\varepsilon}) \sim \exp\left(-\frac{1}{2}(\vec{\varepsilon})^T \mathbf{V}^{-1}(\vec{\varepsilon})\right)$$

When many measurements contribute,

$$\mathcal{L}(\vec{\varepsilon}) \sim \exp\left(-\frac{1}{2}(\vec{\varepsilon})^T \left(\sum_i \mathbf{V}_i\right)^{-1}(\vec{\varepsilon})\right).$$

The covariance matrix $\mathbf{U}_i$ $\mathbf{U}_i = \begin{pmatrix} \sigma^2_{E_{T_i}} & 0 \\ 0 & E^2_{T_i}\sigma^2_{\phi_i} \end{pmatrix}$.

matrix is rotated into the standard CMS $x-y$ reference frame to give the error matrix

$$\mathbf{V}_i = R(\phi_i)\mathbf{U}_i R^{-1}(\phi_i),$$

$$\mathcal{S} = \left(\sum_{i\in X} \vec{E}_{\mathrm{T}_i}\right)^T \left(\sum_{i\in X} R(\phi_i)\mathbf{U}_i R^{-1}(\phi_i)\right)^{-1} \left(\sum_{i\in X} \vec{E}_{\mathrm{T}_i}\right).$$

In the Gaussian case, $\mathcal{S}$ is simply a χ^2 with two degrees of freedom. If we rotate into a coordinate system with the x axis parallel to the $\vec{\not{E}}_{\mathrm{T}}$ axis, instead of the CMS horizontal axis, then Eq. (9) is simplified to $\mathcal{S} = E_T^2/(\sigma^2_{E_T}(1-\rho^2))$, where $\sigma^2_{E_T}$ is the variance of the magnitude of $\vec{\not{E}}_{\mathrm{T}}$, and ρ is the correlation coefficient between the variances parallel to and perpendicular to the measured $\vec{\not{E}}_{\mathrm{T}}$.

Performance of S_{PF} in dijet events

Because S_{PF} is χ^2 distributed, it should exhibit a flat probability of χ^2, $\mathcal{P}(\chi^2)$, for two degrees of freedom in an event sample that nominally has no genuine $\not\!\!E_T$.

- No restrictions were made on the number of interaction vertices in the data, while the simulation has no pile-up

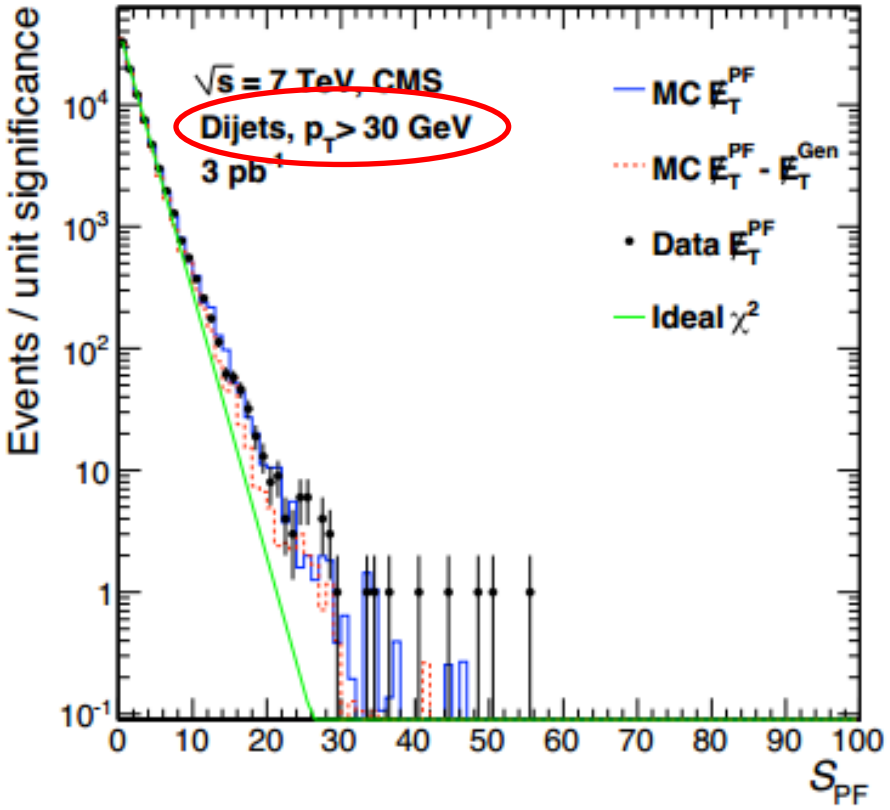

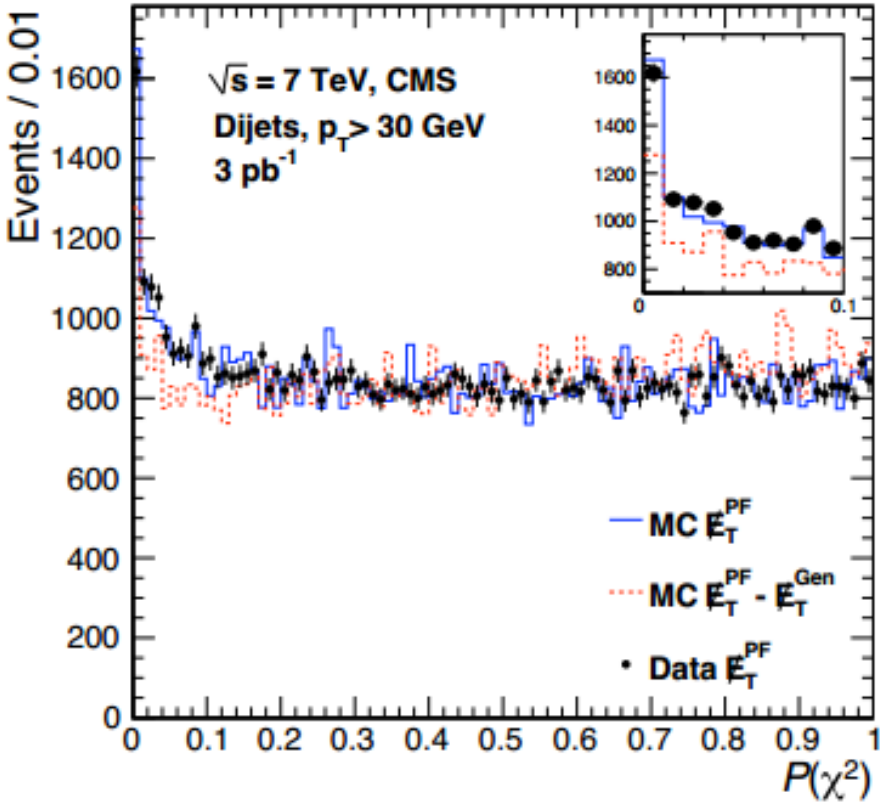

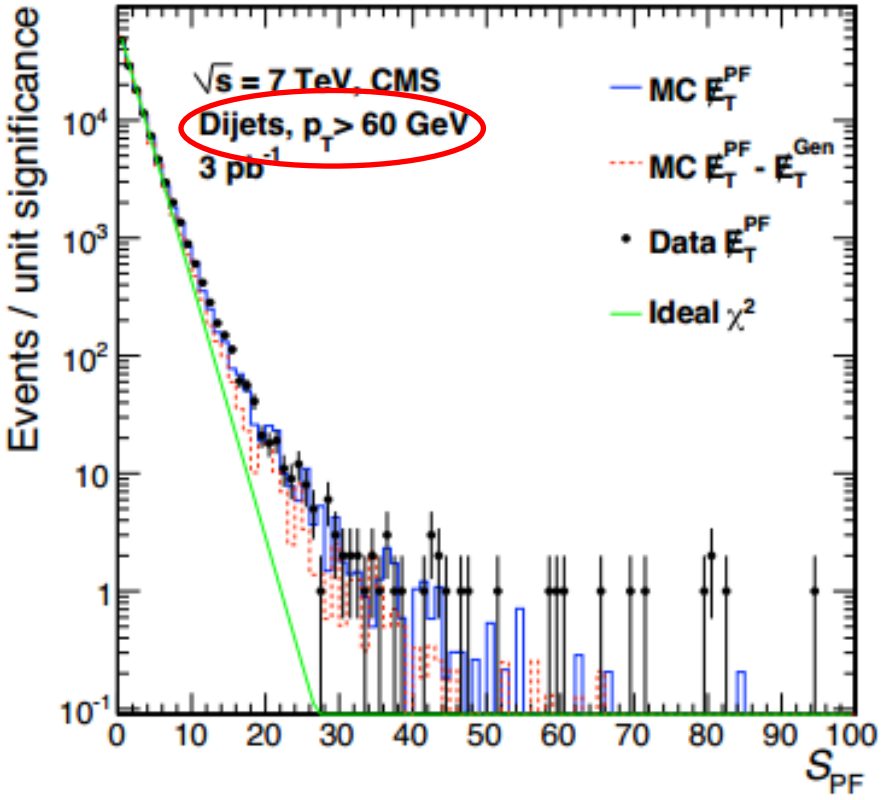
√s = 7 TeV, CMS
Dijets, p_T > 60 GeV
3 pb^-1
MC Ê_T^PF
MC Ê_T^PF - Ê_T^Gen
Data Ê_T^PF
Ideal χ^2
Events / unit significance
S_PF

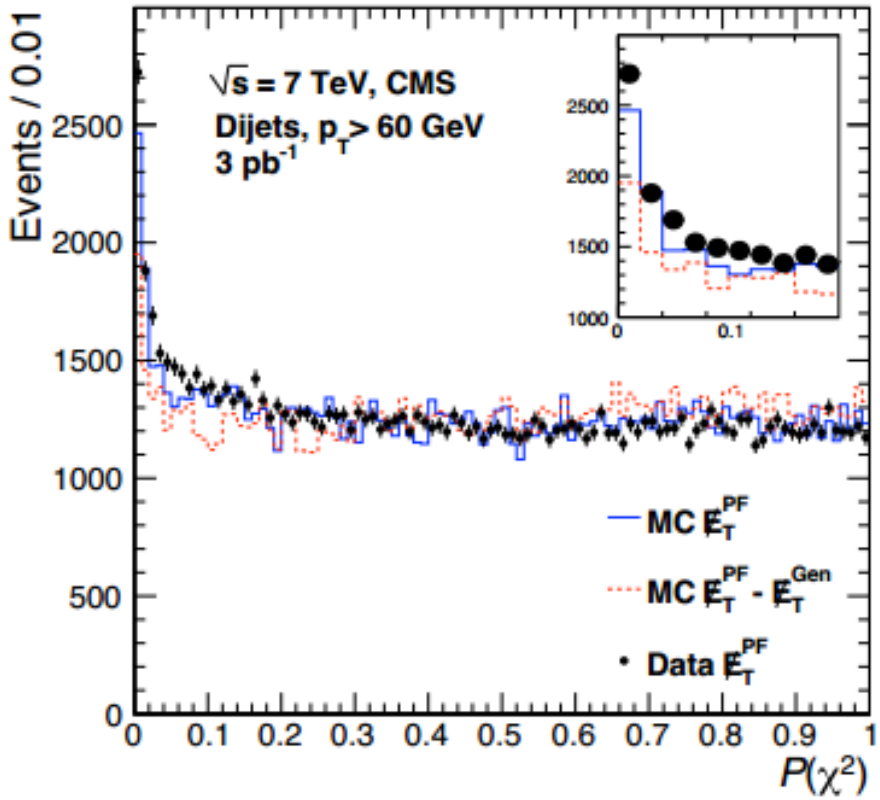
√s = 7 TeV, CMS
Dijets, p_T > 60 GeV
3 pb^-1
MC Ê_T^PF
MC Ê_T^PF - Ê_T^Gen
Data Ê_T^PF
Events / 0.01
P(χ^2)

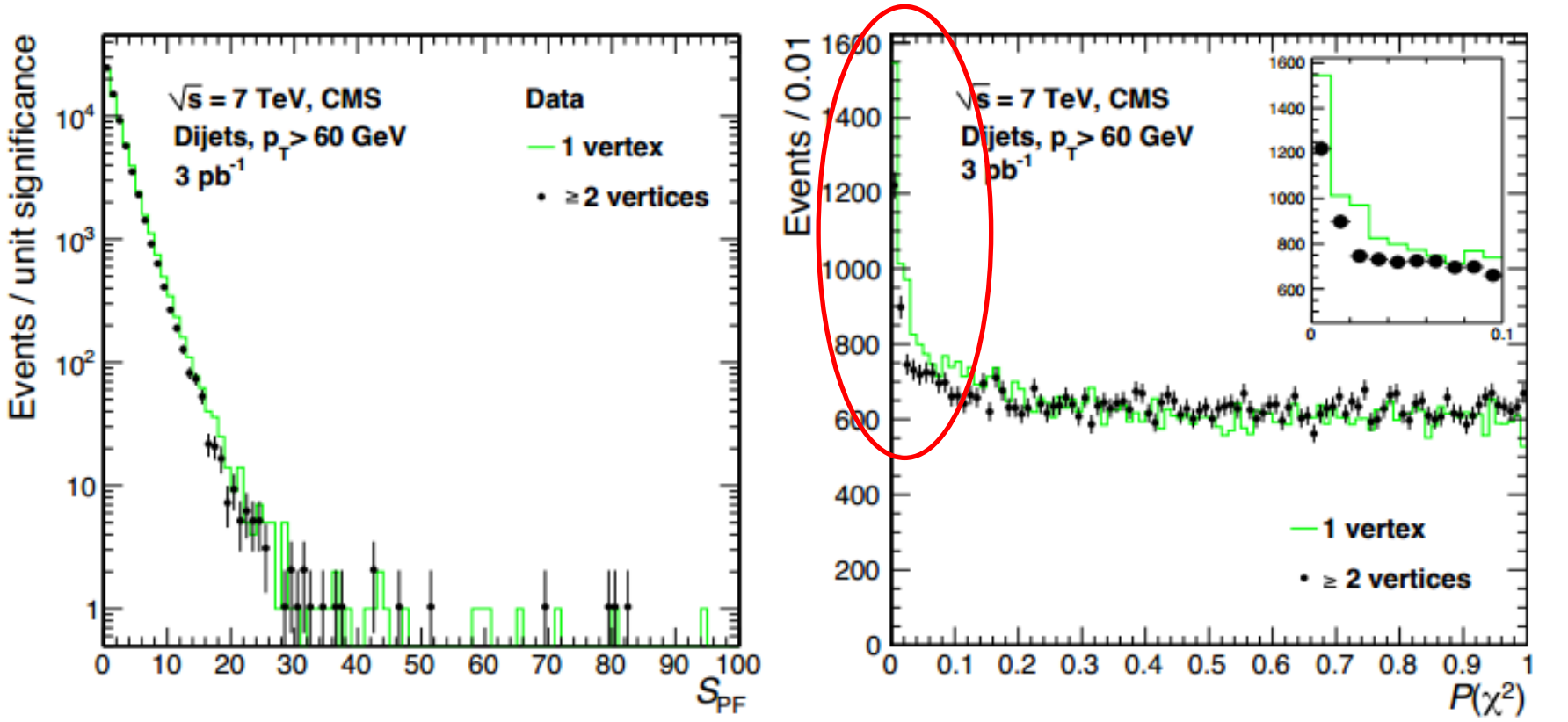

Figure 22: The $\not\!\!E_T$ significance (left) and $\mathcal{P}(\chi^2)$ (right) distributions for events with a single interaction vertex (histogram) and multiple interaction vertices (points) in the 60 GeV threshold dijet sample. The inset expands the small $\mathcal{P}(\chi^2)$ region.

- the multiple interaction data exhibits behaviour closer to the ideal – an example of the central limit theorem

- $\not{E}_T$ and S_{PF} with both the 80% and 95% electron isolation criteria applied
- $\not{E}_T / \sqrt{\sum E_{T_i}}$ with the 95% isolation criteria
- the tighter isolation criterion provides a better signal to background ratio at low background

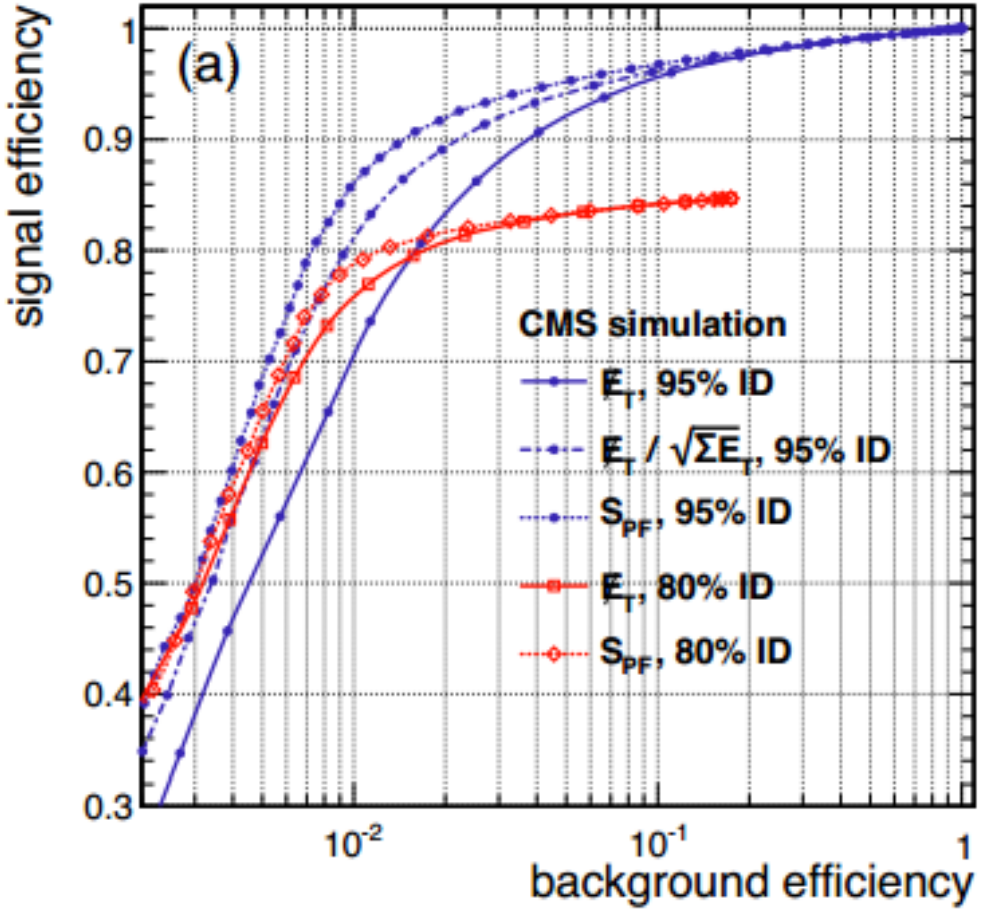

- data and Monte Carlo and see that the agreement is good.
- ,the backgrounds without genuine $\not\!\!E_T$ are compressed towards low values of $\mathcal{S}_{PF}$
- while signal events having real $\not\!\!E_T$ extend to high values of $\mathcal{S}_{PF}$

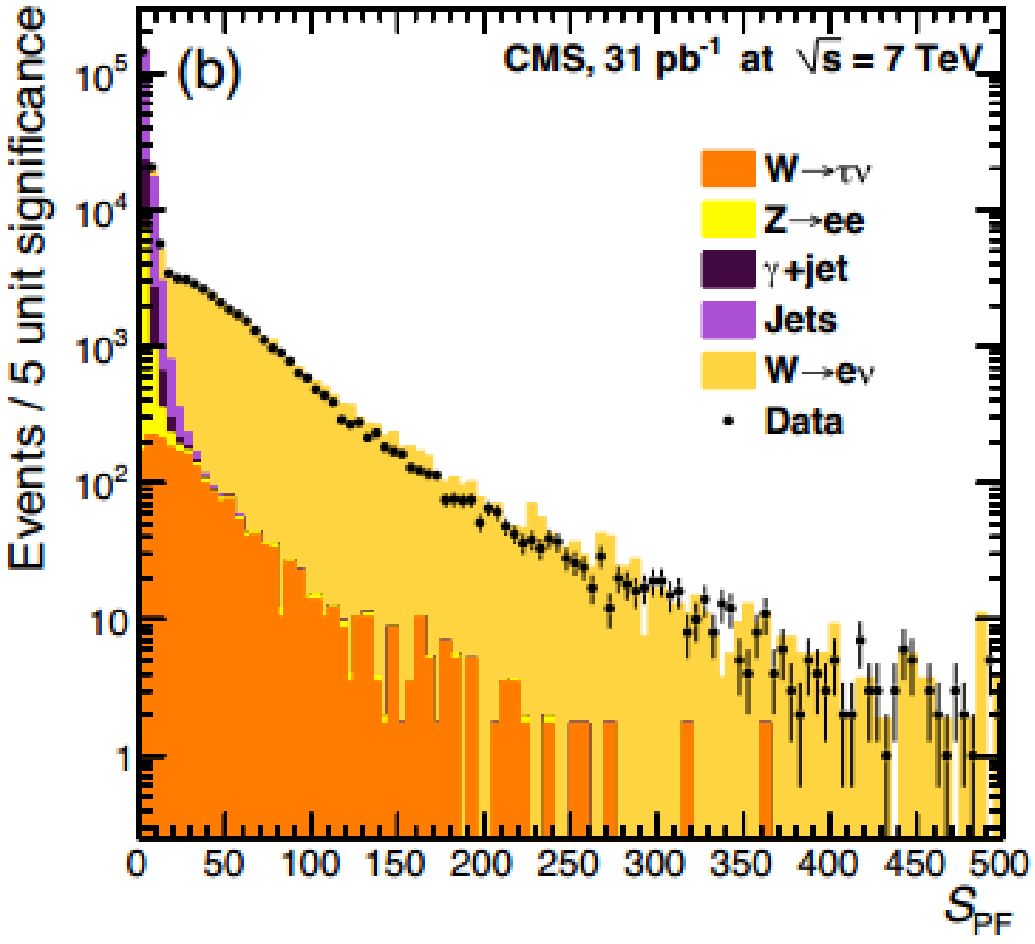

S_{PF} distributions for $W \rightarrow e\nu$

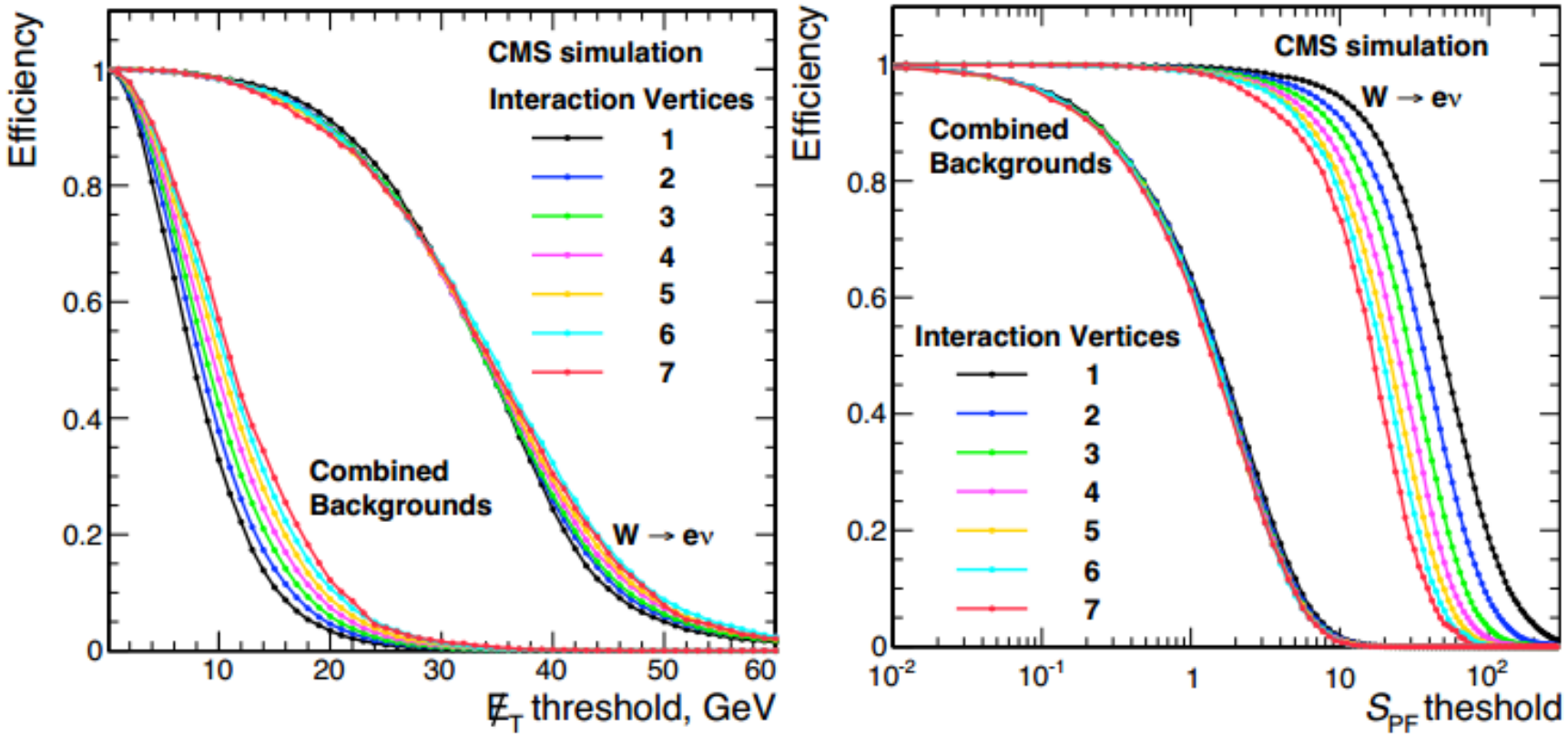

Figure 24: Efficiency versus minimum threshold curves for W → eν signal and for total background for different numbers of interaction vertices with a minimum applied $\not\!\!E_T$ threshold (left) and a minimum applied S_{PF} threshold (right).

- The background contribution at higher $\not\!\!E_T$ grows as pile-up increases, while the S_{PF} levels remain quite stable.
- background subtraction based on extrapolation of $\not\!\!E_T$ will be sensitive to the modeling of pile-up, while one based on extrapolation of S_{PF} would not